Chapter 3
Fluid Pressure Redistribution Events Within a Fault: Impact of Material Property Correlation

Sean A. McKenna and Darin Q. Pike

Abstract Cellular automata (CA) models employ local rules to simulate large-scale behavior. A previously developed CA model of fluid pressure redistribution events within a 2D planar fault system undergoing compression is used to model the size distribution of these events over time. Local fluid pressures exceeding a threshold value cause a rupture (failure) of the surrounding rock, and the fluid pressure is redistributed to surrounding cells. Spatial correlation of the fault compressibility (β) is varied over a range of nearly three orders of magnitude in a model domain of 10^6 cells. The size distribution of all pressure redistribution events changes from a power-law exponential form with a single slope when β is uncorrelated to a power-law exponential form with two slopes at increasing correlation lengths and then back to a single power-law exponential distribution that approximates a uniform distribution as correlation lengths exceed the ergodic limit. The spatially and temporally uniform pattern of events seen in the uncorrelated model rapidly evolve to exhibit emergent behavior as the correlation length increases beyond the grid cell size. Increasing spatial correlation leads to delays in the time to first failure and decreases the time necessary for the ruptures to coalesce and span the fault domain. The resulting spatial pattern of events demonstrates deviations from the random point process associated with uncorrelated β towards increased spatial clustering of events with increasing correlation of the β field. Vertical effective permeability of the fault system at the point where connected failures span the

S.A. McKenna (✉)
Geoscience Research and Applications, Sandia National Laboratories
Currently: IBM Research, Smarter Cities Technology Centre, Bldg-3, Damastown Industrial Estate. Mulhuddart, Dublin 15, Ireland
e-mail: seanmcke@ie.ibm.com

D.Q. Pike
Chemical and Biological Systems, Sandia National Laboratories,
P.O. Box 5800, Albuquerque, NM 87185-073, USA
e-mail: dqpike@sandia.gov

P.K. Mishra and K.L. Kuhlman (eds.), *Advances in Hydrogeology*,
DOI 10.1007/978-1-4614-6479-2_3,

domain shows that effective permeability is a nonlinear function of the correlation length and is strongly controlled by the size (area) of the domain-spanning failed cluster.

3.1 Introduction

The coupled processes of fluid flow and mechanical behavior of rocks in the Earth's crust are important in a number of geologic processes including earthquakes (Claesson et al. 2007; Sarr and Manga 2003; Rojstaczer et al. 1995), geysers (Ingebritsen and Rojstaczer 1993), and crustal-scale fluid flow (Rojstaczer et al. 2008; Miller et al. 2004). Coupled hydromechanical processes are also the focus of a number of research areas driven by engineering applications including CO_2 sequestration (e.g., Rutqvist et al. 2007; Lucier et al. 2006), enhanced geothermal energy production (Majer et al. 2007), and deep borehole injection of fluids (Hsieh and Bredehoeft 1981; Healy et al. 1968; Zoback and Harjes 1997; Rutledge et al. 2004). Here, we examine coupled hydromechanical processes in a fault using a cellular automata model with a focus on the impact of spatially correlated material properties on the evolution of fault system behavior.

The "toggle-switch" permeability model developed by Miller and Nur (2000) considers permeability to be either zero or infinite, and changes between these two extreme states, due to hydraulic fracturing and then resealing, are essentially instantaneous. The fault is conceptualized as a fluid-saturated, two-dimensional planar feature with spatially heterogeneous rock compressibility β. As compressive normal stress is applied to the fault, the spatially heterogeneous β transforms the stress into locally varying amounts of strain as exhibited by changes in the fluid pressure within the fault. If the local fluid pressure exceeds a threshold rupture pressure at any cell, the pressure is redistributed to the surrounding cells; the new pressure is recalculated and again compared to the threshold rupture pressure. The pressure redistribution continues until pressure in all cells is below the threshold pressure. The normal stress continues and the strain is updated at the next time step and the process continues. Miller and Nur (2000) used this model to study how simple small-scale processes can describe the evolution of pore pressures in a fault and lead to the development of large-scale fluid flow networks. Wang and Manga (2010) postulated a process analogous to the toggle-switch idea for rapid changes in the permeability and pore pressure redistribution of a magmatic melt due to earthquake-induced fracturing. Claesson et al. (2007) observed rapid, earthquake-induced changes in ground water flow systems followed by a less rapid fault-sealing process.

To paraphrase the definition of a CA proposed by Mitchell (2009) in the context of the pressure redistribution problem, a CA is a grid of cells, where each cell is in one of two states (e.g., closed/open) depending on the current states of cells within its local neighborhood. The two key components of a CA model are the definition of the local neighborhood and the cell update rule. The cell update rule

defines the state of the cell in the next time step as a function of the states within the neighborhood at the current time step. The cell update rule is identical for all cells at all times (i.e., spatially and temporally stationary). Taken as a whole, CA models have large numbers of simple components that respond to conditions in the local environment without any centralized or hierarchical controller. From these simple cells, having limited intercell communication and all following the same simple, local rule, complex behavior can arise at the macroscale (hundreds of thousands of cells) that is not predictable from consideration of the cell update rule on its own. The resulting macroscale behavior, which is unpredictable given the simple rule set and the initial conditions, is termed "emergent behavior" (Mitchell 2009). We use the toggle-switch model of permeability to demonstrate the evolution of emergent behavior as a function of the spatial correlation length of β.

The CA model of Miller and Nur (2000) is analogous to many statistical physics models that are characterized by initial localized failures that lead to a cascading failure that spans the system (e.g., spring and block models of fracturing; sandpile models of cascading failures; percolation processes for domain-spanning features). We examine behavior of the cellular automata model under the condition of spatially correlated material properties within the fault. This approach expands on previous application of this model where only uncorrelated material properties were studied (Miller and Nur 2000). This approach is contrary to the majority of applications of cellular automata models and studies of self-organized criticality across a wide variety of applications that rely on random uncorrelated properties, perturbations, or failure thresholds (e.g., Ferer and Smith 2011; De Menech et al. 1998; Cowie et al. 1993, 1995; Miller et al. 1996). There are notable exceptions to this assumption of uncorrelated property fields including work on percolation networks with correlation (e.g., Sahimi and Mukhopadhyay 1996). Our approach can be summarized as local (quasi-independent) rules acting on connected (correlated) properties.

In this chapter, we define the CA model and the model of spatial correlation of β within the fault. These two models are used to examine the impact of β spatial correlation on the resulting timing, location, and size distribution of the pressure redistribution events. The size distributions are fit with power-law models having exponential decay at the largest sizes. Changes in the β spatial correlation lead to complex spatial-temporal patterns of events that exemplify emergent behavior. Insights on the impact of β spatial correlation on event initiation and fluid flow patterns within the fault are summarized.

3.2 Cellular Automata Model

A previously developed CA model is used here (Miller and Nur 2000). Conceptually, a two-dimensional fault plane within the Earth's crust is modeled as a lattice of cells. Each cell has a different value of rock compressibility, and normal stresses orthogonal to the fault plane place the fault in compression. The evolution of the fluid pressure within each cell is the quantity of interest. The toggle-switch permeability model is used, meaning that if the pressure in a cell is below a critical

value, it is impermeable with respect to fluid flow ($k \sim 0$, where k is permeability). Above the critical value, the cell is at failure and fluid can immediately migrate into neighboring cells ($k \sim \infty$). This process results in the fluid pressure of all connected cells being equilibrated to the same value. When the pressure of a cell falls below the critical value, it has healed and is again impermeable until a future rupture (see details in Miller and Nur 2000).

The relationship between the change in fluid pressure, P_f, and the plastic deformation or fluid source causing the change is

$$\frac{\partial P_f}{\partial t} = \frac{1}{\phi(\beta_\phi + \beta_f)} \left[\frac{k}{\nu} \nabla^2 P_f - (\dot{\phi}_{\text{plastic}} - \dot{\Gamma}) \right], \tag{3.1}$$

where $\dot{\Gamma}$ is the time-varying fluid source, $\dot{\phi}_{\text{plastic}}$ is the time-dependent porosity reduction, k is the permeability, ν is the fluid viscosity, and ϕ is the porosity. The compressibility of the rock matrix and the fluid are β_ϕ and β_f, respectively. Further details on this pressure diffusion model are given in Segal and Rice (1995) and Walder and Nur (1984).

The "toggle-switch" model of Miller and Nur (2000) limits the permeability values to $k = 0$ and $k \cong \infty$ depending on the local fluid pressure. Under the zero permeability mode ($k = 0$), pressure redistribution by diffusion does not occur and the following simplified pressure differential is used:

$$\left. \frac{\partial P_f}{\partial t} \right|_{\text{noflow}} = \frac{(\dot{\Gamma} - \dot{\phi}_{\text{plastic}})_i}{\phi_i \beta_i}, \tag{3.2}$$

where P_f is the pressure in the ith cell at time t and β_i is the sum of matrix and fluid compressibility for cell i. In the calculations to follow, $(\dot{\Gamma} - \dot{\phi}_{\text{plastic}})_i$ is constant throughout time and space. A constant ϕ is employed and β is varied across the domain making the spatial correlation of β the focus in the remainder of the chapter.

Prior application of the toggle-switch model to pressure redistribution considered either $(\dot{\Gamma} - \dot{\phi}_{\text{plastic}})_i$ or $\phi_i \beta_i$ within each cell to be independently drawn from a uniform or Gaussian distribution (Miller and Nur 2000). Here, we follow this approach by drawing β_i from a Gaussian distribution while adding spatial correlation between the cells defined through a Gaussian kernel (see below).

At each time step, a constant compressional strain increases P_f by decreasing ϕ_{plastic} within each cell through Eq. (3.2). When P_f in a cell reaches a threshold pressure, P_{thresh}, the cell "fails," permeability suddenly increases from 0 to infinity, and the pressure is redistributed to the four adjacent cells. Each cell within this neighborhood $(m = 4)$ is then assigned the same weighted average pressure, computed as

$$\bar{P} = \frac{\sum_{i=1}^{m} (\phi\beta)_i P_i}{\sum_{i=1}^{m} (\phi\beta)_i}. \tag{3.3}$$

Equation (3.3), coupled with the threshold pressure, is the cell update rule for the CA model. Here, the local neighborhood for the CA model is defined as the 4 adjacent (non-diagonal) cells in the grid. After the pressure redistribution, if all cells are below the critical pressure, the system proceeds to the next time step via Eq. (3.2). If, on the other hand, there are still cells with $P_f > P_{\text{thresh}}$, the pressure redistribution process is repeated until $P_f \leq P_{\text{thresh}}$ in all cells. The size of a pressure redistribution event is measured as the number of cells involved in the pressure redistribution starting from a single cell with $P_f > P_{\text{thresh}}$ until all cells are below P_{thresh}. Many of the cells involved in the redistribution event never reach failure; they are only involved in the redistribution of the fluid pressure. These "event clusters" differ from the definition of failure clusters of Miller and Nur (2000), where all cells in the cluster must have reached failure at some point. The event cluster plots have the same behavior as the failure cluster plots, but with larger sizes. Event clusters are used here to be consistent with fluid pressure as the primary object of study.

3.3 Spatial Correlation

Statistical physics models typically apply local rules to fields of uncorrelated properties. From application of these rules, a spatial correlation in the resulting state arises. A classic example of this behavior is the standard percolation model (Stauffer and Aharony 1994). The probability of any cell in the domain being conductive is a random variable with correlation length equal to that of the grid spacing leading to an uncorrelated random field. As the probability threshold for turning any cell in the domain to being conductive increases, a point is reached where a connected path of conducting cells spans the domain. At this point, the domain is said to "percolate" and the correlation length of the percolating cells relative to the domain size is now infinite.

Here, we examine the impact of another correlation length, that of the material properties on which the CA rules operate, on the overall results of the CA model. Spatial correlation is imposed on β by averaging a white-noise (uncorrelated) multivariate Gaussian field with a kernel. Here the kernel, $G(x,y)$, also has a Gaussian shape and the resulting correlated fields are also multivariate Gaussian:

$$G(x,y) = \frac{1}{2\pi\,|\Sigma|^{\frac{1}{2}}} \exp\left(-\frac{1}{2}\mathrm{d}\Sigma^{-1}\mathrm{d}^{T}\right), \tag{3.4}$$

where d is the Euclidean distance vector (d_x, d_y) from any point to the origin of the Gaussian function. For the isotropic fields considered here, the covariance matrix $\Sigma = \sigma^2 I$, where I is the identity matrix and σ is the standard deviation of the Gaussian kernel, is diagonal because the kernel is aligned with the grid axes. The measure of the correlation length of the resulting field is the full width at half

maximum, δ, defined as $\delta = \sigma\sqrt{8\ln(2)}$. This is the width of the Gaussian kernel used to create the correlated field at one-half the maximum kernel height. For each δ, 15 individual realizations of the β field are created and used as input to the CA model.

3.4 Results

Calculations were conducted on a grid of 1.0×10^6 $(1{,}000 \times 1{,}000)$ cells. Although no explicit scale is assigned here, this model domain could be considered representative of a fault domain of tens to hundreds of meters on a side. The initial pressure of each cell was independently set to a random number between 15 and 16 MPa—an elevation-dependent starting pressure is not considered. The failure condition was set to 28 MPa, an overburden pressure representative of an approximate 1.5 km depth. The time step used was $dt = 0.1$ year, and the numerator of Eq. (3.2) $(\dot{\Gamma} - \dot{\phi}_{\text{plastic}})$ was set to 1×10^{-5} year $^{-1}$ for all cells. The values of β_i had a mean of $0.01\,\text{MPa}^{-1}$ and standard deviation of $0.0025\,\text{MPa}^{-1}$ where $\phi = 0.02$ and all spatial variation is due to β.

Calculations were run with the following full width at half maximum values: $\delta =$ 0.39, 2.35. 4.71, 9.42, 18.8, 23.5, 47.1, 94.2 188, 235, and 471 grid cells. The lowest δ value, 0.39, represents the uncorrelated case where the value of β_i at each cell is independent of its neighbors. The uncorrelated case is consistent with each cell encompassing 99.7% of the full width ($\pm 3\sigma$) of the Gaussian kernel. Four example β fields are shown in Fig. 3.1.

For each of the 165 input β fields (15 realizations for each of 11 values of δ), the CA model simulations were run from the initial pressure conditions until a domain-spanning cluster of failed cells was reached. At every time step, the coordinates of the centroid of the pressure redistribution event and the event (cluster) size in terms of grid cells are recorded. Additionally, the final spatial distribution of the failed and intact rock as well as the failed rock that is connected to the domain-spanning cluster is recorded. Figure 3.2 shows example results from compressibility fields with three correlation lengths: 0.39, 9.4, and 94 units. The spatial-temporal distribution of the events is summarized in a two-dimensional plot by only showing the vertical (y-dimension) location of each event as a function of time (Fig. 3.2). The time in these plots has been normalized between the start of the simulation and the onset of the domain-spanning cluster.

The domain-spanning clusters in the left column of Fig. 3.2 show that as δ increases, the nature of the clusters changes substantially. At the lowest δ value (Fig. 3.2, upper left), the cluster is rough-edged and surrounds isolated regions of intact rock with a range of sizes. The black region is not at all continuous, containing within it many intact (white) regions of various size as well as other smaller, disconnected regions of failed rock (grey). In general, the domain-spanning cluster and the regions of contained intact and failed rock occurring at multiple

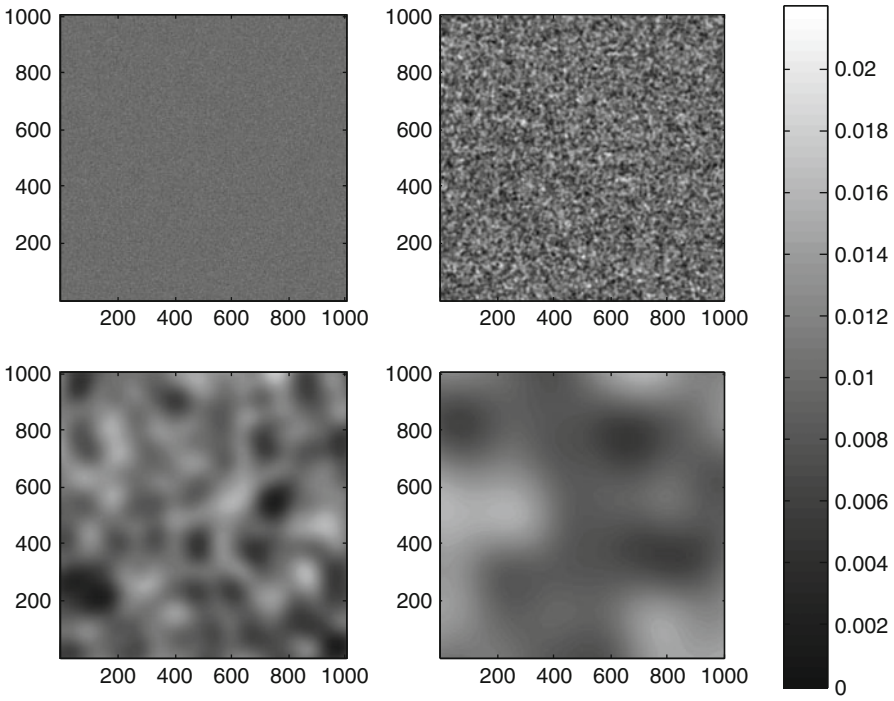

Fig. 3.1 Example of four realizations of the β field showing four different correlation lengths. The values of δ are 0.39 (*upper left*), 9.4 (*upper right*), 94 lower left, and 235 (*lower right*). The color scale is in units of 1/MPa

scales resemble a fractal object. Results from the next largest δ shown in Fig. 3.2 (9.4 cells) similarly show the domain-spanning cluster surrounding regions of white and grey, with less variability in the size distribution of these surrounded regions. Notably, there are no small white regions mixed evenly within the black as seen in the upper image. Finally, at the largest δ value (94 cells), the domain-spanning cluster is almost completely uninterrupted, with the exception of a single enclosed area of intact (white) rock. There are only a few grey regions in the entire image. The perimeter to area ratio of the domain-spanning cluster decreases as δ increases.

The spatial-temporal evolution of the events is summarized in the right column of Fig. 3.2. For the uncorrelated case (upper image), there are 10–12 locations that fail repeatedly over time plus additional events that occur at apparently random locations. The intensity of these randomly located events increases with increasing time until the domain-spanning cluster is formed. In general, the events appear to remain local and have little impact on the formation of events in surrounding locations. As δ increases to 9.4 cells (middle image), the pattern is similar to the uncorrelated case with more locations (25–30) having early failures that repeat continuously through time along with a more abrupt increase in the density of the randomly located events at late times relative to the uncorrelated case. Additionally,

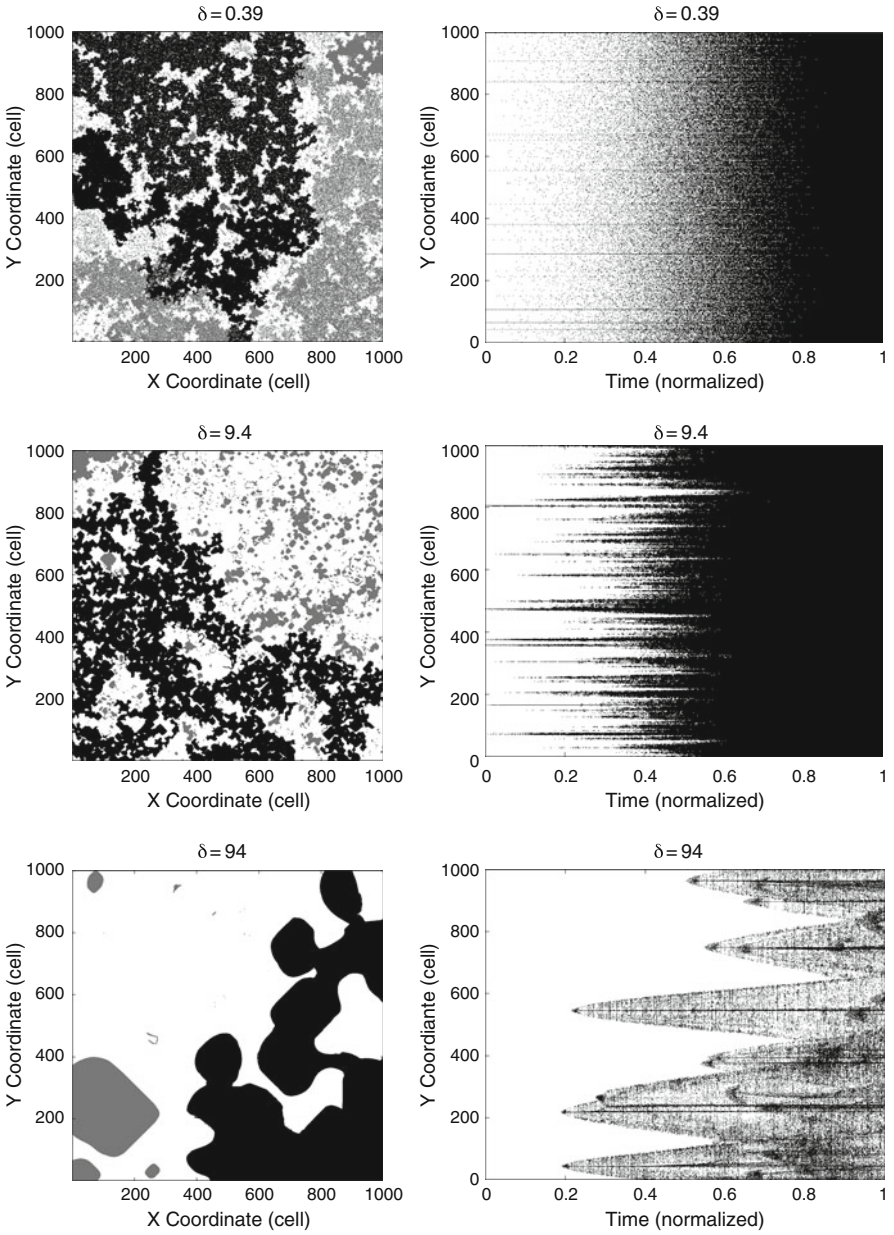

Fig. 3.2 For three different values of $\delta(0.39, 9.4$, and 94, *top to bottom*) the images on the left show the areas of rupture in *black and grey* at the time when the domain-spanning ruptured region is reached. Cells within the domain-spanning cluster are *black*, other ruptured cells are *grey*, and intact rock is *white*. *On the right*, the y-coordinate of the centroid of each rupture event is plotted vs. normalized time, where time ranges from the start of the simulation to the point where the ruptured material spans the domain, as illustrated in the images *on the left*

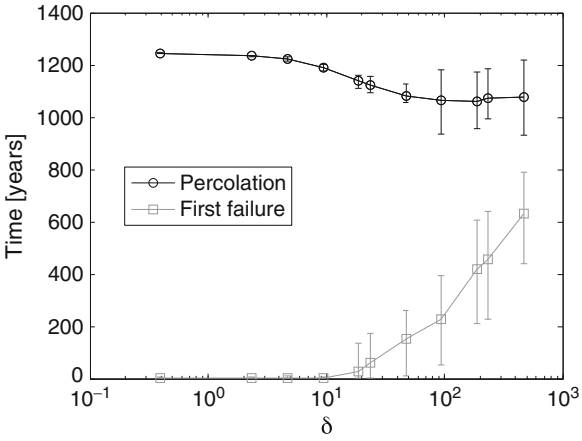

Fig. 3.3 The time to first failure and the time at which the ruptured region achieves percolation across the domain. For each value of δ, averages over the 15 realizations are plotted (*circles and squares*) along with the minimum and maximum values

the size of the neighborhood of locations where the failures are nearly continuous from early time grows as time increases indicating an outward growth of the failure locations from an original single nucleation point. At the largest δ (94 cells) in the lower image, the pattern changes markedly such that there are a relatively small number (10–12) of locations with repeating failures. A halo of failure locations moves outward from these repeating locations as time increases and all failures occur within one of these halos—there is no random component of failure locations outside of these halos. There is a significant delay in the time to first failure relative to the results from the smaller δ values; in this example, the first failure does not occur until 20% of the simulation time has passed. These unexpected complex patterns arising from operation of simple local rules on increasingly correlated material property fields signify emergent behavior in fluid pressure redistribution events.

Figure 3.3 plots the time to first failure, the first point when any cell has a pressure above the failure threshold (28 MPa), and the time to reach the domain-spanning (bottom to top) cluster. Since all cells start with similar pressures, the cells with the smaller values of β_i fail first. Increasing spatial correlation acts to increase the time to the first rupture and decrease the time to reach the domain-spanning cluster. These results show that correlated fields of rock compressibility can accommodate more strain before failing than can uncorrelated fields, but once failure is initiated, there is a more rapid progression to domain-spanning failure relative to the uncorrelated case.

For δ values up to 10.0 units, the initial failure occurs nearly instantaneously as the strain begins and there is no variation in this value between realizations. Above a δ of 10.0, the initial failure is delayed to times beyond the initiation of strain. Additionally, the variability in this time to initial rupture is nearly ± 200 years across the realizations for each δ. The variability in the results between realizations becomes considerable as δ reaches one-tenth of the domain length ($\delta = 100$). As a rule of thumb, a correlation length of one-tenth the domain size is the ergodic limit.

As correlation lengths go beyond this limit, the statistics (e.g., the mean β) are no longer constant from one realization to the next creating increased inter-realization variability as seen here (see additional details on ergodic limits in Zhang 1999).

At each time step, each percolation cluster is recorded with its size. For each value of δ, the number of clusters of each size is counted, summing over all time steps up to the point of domain-spanning cluster formation. All 15 realizations are aggregated, and these results are used to produce curves of the complementary cumulative distribution function (1—CDF) in log–log space. Similar curves were produced by Miller and Nur (2000), but their failure clusters were used instead of event clusters, as noted previously. The event cluster curves are nearly identical to failure cluster curves in terms of slope; they are merely shifted to the right. In the case of uncorrelated values of β, the cluster size distribution value as a function of cluster size, $D(S)$, can be fit to (Miller and Nur 2000):

$$D(S) = S^{-\alpha} \exp\left(-\frac{S}{L}\right), \tag{3.5}$$

where S is the cluster size, α is the power-law exponent, and L is a correlation length distinct from δ. Both α and L are fit to the data. The best fit is obtained with $f(\alpha, L) = \log(D)$ using the Matlab function nlinfit (MATLAB 2011). To accurately fit results with Eq.(3.5), the data must first exhibit linear behavior on the log-log plot with slope of -α followed by an exponential decay at the largest sizes. This equation does not provide the best fit to the data from correlated fields, especially at larger values of δ. A noticeable deviation between these data and Fig. 3.8 of Miller and Nur (2000) is that approximately 30%–50% of their clusters have size $S = 2$. Here, there are no clusters of size $S = 2$ due to the redefinition of clusters and only a negligible amount of them have size $S = 3$ or $S = 4$ (due to edge artifacts), and the most frequently observed size is $S = 5$ consistent with the 5-point star pattern used in the pressure redistribution process.

The results in Fig. 3.4 show the size distribution of the rupture events. As δ increases, this distribution changes from a power-law model with exponential roundoff at the largest sizes to a double power law with exponential roundoff and finally back to the original single power law with exponential roundoff, but a much shallower slope than the models for smaller δ values. Especially at higher values of δ, it can be seen that the slope of the linear section changes prior to the onset of exponential decay.

In order to better fit the results across the range of δ values, a piecewise function with two power-law slopes prior to the exponential decay was constructed:

$$D(S) = \begin{cases} cS^{-\alpha_1} \exp\left(-\frac{S}{L}\right) \exp\left(\frac{1}{L}\right) & \text{if } S \le \gamma, \\ cS^{-\alpha_2} \gamma^{\alpha_2 - \alpha_1} \exp\left(\frac{S}{L}\right) \exp\left(\frac{1}{L}\right) & \text{if } S \ge \gamma. \end{cases} \tag{3.6}$$

Compared to Eq. (3.5), α has been split into α_1 and α_2, and additional dependent variables, c and γ, have been introduced. γ is the value of S where the change in

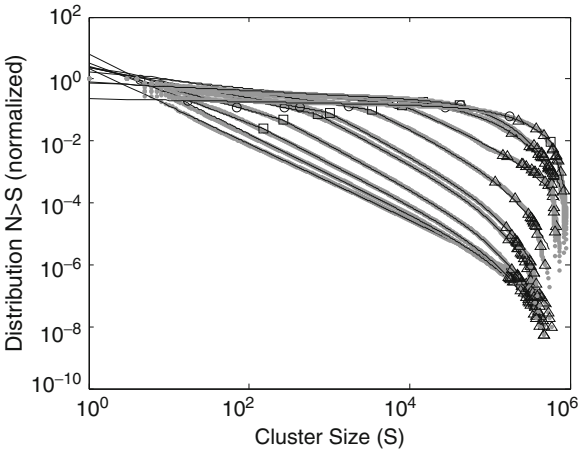

Fig. 3.4 Distributions of cluster sizes for each δ value. The size distribution curves shift to the top right corner as δ increases. For each δ, the data points are *grey*, the equation fit is *black*, the point of change in slope (γ) is a *square*, the δ related area is a *circle*, and the maximum cluster size for each individual realization is a *triangle*. For each δ, each distribution is calculated over all 15 realizations

Table 3.1 Variables c, α_1, α_2, L, and γ from Eq. (3.6) are fit to match the cluster size data produced. The coefficient of determination, R^2, is included for each δ. Also included is the characteristic size of the compressibility field calculated as the area of a circle with diameter $\delta : \pi(\delta/2)^2$

δ	c	α_1	α_2	L	γ	$\pi(\delta/2)^2$	R^2
0.392	2.25	–	1.22	370,000	0	0.121	0.9996
2.35	6.38	–	1.29	144,000	0	4.36	0.9990
4.71	3.26	0.972	1.35	111,000	150	17.4	0.9997
9.42	2.63	0.717	1.41	103,000	266	69.7	0.9998
18.8	2.30	0.525	1.39	99,100	710	279	0.9995
23.5	2.29	0.482	1.40	110,000	1,010	436	0.9996
47.1	2.32	0.386	1.30	150,000	3,350	1,740	0.9983
94.2	1.71	0.273	1.14	384,000	8,120	6,970	0.9926
188	0.778	0.145	0.427	147,000	14,600	27,900	0.9917
235	0.756	0.128	0.481	151,000	42,400	43,600	0.9974
471	0.230	0.0481	5.81	227,000	582,000	174,000	0.9941

slope from α_1 to α_2 occurs. The factor $\exp(1/L)$ has been added to ensure $D(1) = c$. While the actual data will always be $D(1) = 1$, there are very few data points at $S = 1$ and not restricting the model to go through this point by introducing the variable c improves the overall fit. However, the model should be used for $S \geq 5$, the size of the pressure redistribution stencil, to avoid spurious results. When $S \leq \gamma$ the log-log plot yields a slope of -α_1. When $S \geq \gamma$ the slope changes to -α_2 and then decays exponentially for the largest S. The function is continuous, but there is a discontinuity in the slope at $S = \gamma$. This function is recast using an approximation of the Heaviside function for parameter estimation using the Matlab *nlinfit* function (MATLAB 2011). The resulting fits of Eq. (3.6) to the size distributions are shown in Fig. 3.4. The parameters used to fit the size distributions are shown in Table 3.1.

Equation (3.6) provides excellent fits ($R^2 > 0.99$) to the observed size distribution for all values of δ. Up to the point of reaching the ergodic limit ($\delta \sim 100$), the quantity $\pi(\delta/2)^2$ provides a reasonable lower bound on the estimated value of γ; however, decreasing the number of estimated parameters by replacing γ with $\pi(\delta/2)^2$ decreased the goodness of fit. The values of α_1 define a decreasing negative slope with increasing δ. The values of α_2 remain above 1.0 and are relatively constant up to the ergodic limit where they begin to decrease (a less negative slope). The value of α_2 at $\delta = 471$ is somewhat of an outlier as it does not take effect until the curve is already into the exponential decay region. In all cases, the piecewise curve fits the data better than the single power-law function (3.5). The curves produced from the data in Table 3.1 are plotted in Fig. 3.4 along with the original data. The maximum cluster size for each realization is highlighted.

Figure 3.4 shows that for the uncorrelated case ($\delta = 0.39$), 99% of all events have a size of 100 cells or less, whereas for a correlation length of $\delta = 94$, 99% of the events have a size of 10,000 cells or less. This result shows the size distribution moving from a power-law distribution ranging over multiple orders of magnitude to a distribution closer to uniform with an exponential decay at the highest end. This behavior is indicative of a wide range of cluster sizes merging to create a domain-spanning cluster in an uncorrelated field and a much more uniformly sized set of clusters joining to create the domain-spanning cluster at larger values of δ.

The spatial patterns of the event centroids are compared to a completely random spatial point process using the distribution of nearest neighbor distances between events at each time step. Specifically, the event locations are compared to the case of complete spatial randomness (CSR). To satisfy CSR, data points must be an uncorrelated random sample from a uniform distribution. When this is the case, the nearest neighbor distance from a data point, r, on average is (Diggle 2003)

$$\mu = 0.5(n^{-1}A)^{\frac{1}{2}} + (0.051 + 0.042n^{-\frac{1}{2}})n^{-1}P, \tag{3.7}$$

where μ is the expected value of r, n is the number of data points, A is the area of the region considered, and P is its perimeter. As soon as observed patterns emerge, CSR is no longer present.

Figure 3.5 shows the results of this analysis for three example simulations, with the right image of Fig. 3.5 showing a closer look at the last half of the simulation time. The y-axis shows the difference between the mean observed r and μ. In the uncorrelated case, the difference is near zero for the majority of the simulation. At 95% of the simulation time, there is a slight deviation towards negative values indicating a slight clustering of the events. Results with a δ of 9.4 show moderate spatial clustering of the events throughout the simulation until very near the end when they become more spatially random. With a δ of 94, the spatial clustering is extreme for the first 50% of the simulation and then moves towards a more random pattern at the end. The results with $\delta = 94$ show considerable variability with large increases and decreases in the difference throughout time. Only events created under

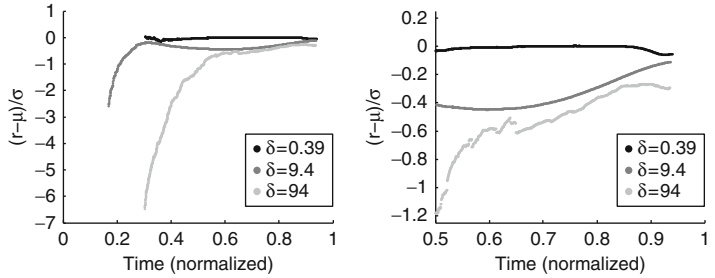

Fig. 3.5 Results of the spatial clustering analysis for three example realizations at three different δ values. The *right image* is a zoomed in portion of the *left image*. Values near zero indicate spatial randomness, while positive and negative values indicate regularity and clustering, respectively

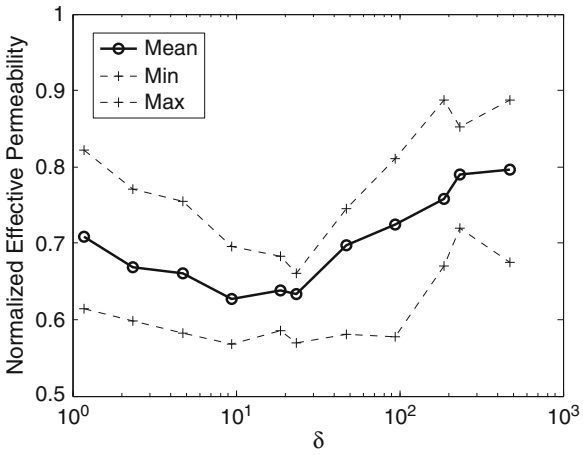

Fig. 3.6 Normalized effective fault permeability (*vertical*) as a function of δ. The mean, minimum, and maximum values across 15 realizations are shown for each δ. The effective values are normalized by the permeability value assigned to the failed rock

the uncorrelated case fit the pattern of complete spatial randomness throughout the simulation.

The failure patterns within the fault at the point of domain-spanning percolation are used to examine the effective permeability (vertical) of the fault. Steady-state, single-phase, isothermal flow is simulated across the fault in the vertical direction and the applied gradient and resulting flux are used to calculate the effective permeability. The permeability of the failed regions is set to be four orders of magnitude higher than that of the intact regions and the effective permeability of the fault domain is normalized by the permeability value assigned to the failed regions (Fig. 3.6). The connected high-permeability path across the fault ensures that all mean effective permeability values are at least 60% of the maximum permeability assigned to the failed regions.

For the uncorrelated case, the mean effective permeability is just over 70% of the failed region permeability. The minimum mean effective permeability value occurs at $\delta = 9.42$ before rising again to a maximum of near 80% of the failed region

permeability for $\delta = 492$. This behavior is controlled by the proportion of the fault domain that is contained within the spanning cluster, which also reaches a minimum at $\delta = 9.42$. At lower δ values, the spanning cluster is larger and complex with multiple continuous pathways connecting the top and bottom boundaries as well as many intact rock fragments contained within, or surrounded by, the spanning cluster (e.g., Fig. 3.2, top left image). At δ values of 9.42, the number of pathways connecting the top and bottom boundaries of the fault decreases to near 1 (e.g., Fig. 3.2, center left image) causing decreased mean effective permeability. For larger values of δ, a single connected pathway remains, but it is larger and less complex, containing less intact material, than at lower values of δ (e.g., Fig. 3.2, bottom left images). Emergence of a single dominant flow path at larger correlation lengths is consistent with results of Pyrak-Nolte and Morris (2000) in a study of fracture stiffness and fluid flow.

3.5 Conclusions

Geologic media are commonly observed to have spatially correlated material properties. In particular, within a fault, prior movement along the fault and a changing stress history will lead to zones of preferential strength and weakness. Simulation of pressure redistribution events within a fault using a CA model clearly shows the impact of rock compressibility (β) spatial correlation on both the size distributions and the spatial and temporal patterns of the pressure redistribution events.

Increasing the spatial correlation (δ) of β leads to a field that can sustain larger amounts of strain prior to the first failure. Higher δ values also decrease the time until a fault-spanning cluster of failed material is achieved. As δ increases, the more uniform distribution of event sizes leads to higher numbers of larger events and faster connection of failed regions across the fault relative to the uncorrelated case. Once a location ruptures, the surrounding area, having a similar compressibility, is already at a similar fluid pressure and therefore the excess pressure is quickly redistributed to the edge of this region and new ruptures occur in material with a higher compressibility (more compliant material). This process results in the "halo" effect of a central rupture location surrounded by a ring of associated failures (see Fig. 3.2 center and bottom right images). The final pattern of intact and failed regions within the fault results in an effective permeability for the fault that is a nonlinear function of δ. At small to moderate δ, the failed region is complex and more poorly connected than for the uncorrelated case leading to a minimum value of the effective permeability. At the largest δ, a dominant, uninterrupted failed region emerges that maximizes the fault effective permeability.

In almost all applications of CA models and other studies of self-organized criticality, the material properties are represented as uncorrelated random fields. This study demonstrates that local rules in a CA model operating on correlated

properties lead to emergent behavior. This behavior is significantly different from that seen on the standard uncorrelated fields. The emergent behavior identified here is the evolution of increasingly complex spatial-temporal patterns of failure within the fault as exemplified in the right-hand side of Fig. 3.2. As the amount of spatial correlation increases, the event size distribution changes from a single power law to a double power law and then back to a single power-law distribution. The slope for the initial power law in the cases with double power-law behavior is always shallower than for the case of uncorrelated material properties. In all cases, the largest events fit a distribution model with exponential tailing.

The simulations done here are for rock compressibility fields with isotropic spatial correlation. Future simulations will look at the impact of anisotropic correlation patterns as may result from normal or strike-slip displacement along the fault. The multivariate Gaussian model adopted here for the random fields is parametrically and computationally efficient, but other, non-Gaussian, field models may better represent aspects of observed faults. This study uses a CA model with several simplifying assumptions to evaluate the impact of material property correlation on fluid pressure redistribution. Some of those assumptions including conceptualization of permeability as only being zero or infinite and the closed boundary conditions should be reevaluated in future studies. Field observations of earthquake activity in faults with high fluid pressures and microseismic activity at subsurface injection sites should be able to provide information that can distinguish between the independent and correlated property field models examined here.

Acknowledgements This material is based upon work supported as part of the Center for Frontiers of Subsurface Energy Security, an Energy Frontier Research Center funded by the US Department of Energy, Office of Science, Office of Basic Energy Sciences under Award Number DE-SC0001114. Sandia National Laboratories is a multiprogram laboratory managed and operated by Sandia Corporation, a wholly owned subsidiary of Lockheed Martin Corporation, for the US Department of Energy's National Nuclear Security Administration under contract DE-AC04–94AL85000.

References

Claesson L, Skelton A, Graham C, Morth C-M (2007) The timescale and mechanisms of fault sealing and water-rock interaction after an earthquake. Geofluids 7(4):427–440

Cowie PA, Sornette D, Vanneste C (1995) Multifractal scaling properties of a growing fault population. Geophys J Int 122:457–469

Cowie PA, Vanneste C, Sornette D (1993) Statistical physics model for the spatiotemporal evolution of faults. J Geophys Res 98(B12):21,809–21,821

De Menech M, Stella AL, Tebaldi C (1998) Rare events and breakdown of simple scaling in the abelian sandpile model. Phys Rev E 58(3):R2677–R2680

Diggle PJ (2003) Statistical analysis of spatial point patterns, 2nd edn. Oxford University Press, Oxford

Ferer M, Smith DH (2011) Characterising the correlations of failure events: A 2-D Block-and-Springs model. Strain 47(2):187–195, doi:10.1111/j.1475–1305.2010.00758.x

Healy JH, Rubey WW, Griggs DT, Raliegh CB (1968) The Denver earthquakes. Science 161(3848):1301–1310

Hsieh PA, Bredehoeft JD (1981) A reservoir analysis of the Denver earthquakes: a case study of induced seismicity. J. Geophys Res 86: 903–920

Ingebritsen SE, Rojstaczer SA (1993) Controls on geyser periodicity. Science 262(5135):889–892

Lucier A, Zoback M, Gupta N, Ramakrishnan TS (2006) Geomechanical aspects of CO2 sequestration in a deep saline reservoir in the Ohio River Valley region. Environ Geosci 13(2): 85–103

Majer EL, Baria R, Stark M, Oates S, Bommer J, Smith B, Asanuma H (2007) Induced seismicity associated with Enhanced Geothermal Systems. Geothermics 36:185–222

MATLAB (2011) The MathWorks Inc., version 7.13.0, Natick, Massachusetts

Miller SA, Collettini C, Chiaraluce L, Cocco M, Barchi M, Kaus BJP (2004) Aftershocks driven by a high pressure CO2 source at depth. Nature 427:724–727

Miller SA, Nur A (2000) Permeability as a toggle switch in fluid-controlled crustal processes. Earth Planet Sci Lett 183(133):146

Miller SA, Nur A, Olgaard DL (1996) Earthquakes as a coupled shear stress – high pore pressure dynamical system. Geophys Res Lett 23(2):197–200

Mitchell M (2009) Complexity: a guided tour. Oxford University Press, Oxford, 349 p

Pyrak-Nolte LJ, Morris JP (2000) Single fractures under normal stress: The relation between fracture specific stiffness and fluid flow. Int J Rock Mech Min Sci 37:245–262

Rojstaczer S, Ingebritsen SE, Hayba DO (2008) Permeability of the continental crust influenced by internal and external forcing. Geofluids 8:128–139

Rojstaczer S, Wolf S, Michel R (1995) Permeability enhancement in the shallow crust as a cause of earthquake-induced hydrological changes. Nature 373:237–238

Rutledge JT, Phillips WS, Mayerhofer MJ (2004) Faulting induced by forced fluid injection and fluid flow forced by faulting: an interpretation of hydraulic-fracture microseismicity, carthage cotton valley gas field. Texas. Bull Seismol Soc Am 94(5):1817–1830

Rutqvist J, Birkholzer J, Cappa F, Tsang C-F (2007) Estimating maximum sustainable injection pressure during geological sequestration of CO_2 using coupled fluid flow and geomechanical fault-slip analysis. Energ Conserv Manag 48:1798–1807

Sahimi M, Mukhopadhyay S (1996) Scaling properties of a percolation model with long-range correlations. Phys Rev E 54:3870–3880

Sarr MO, Manga M (2003) Seismicity induced by seasonal groundwater recharge at Mt. Hood, Oregon. Earth Planet Sci Lett 214:605–618

Segal P, Rice JR (1995) Dilatancy, compaction, and slip instability of a fluid infiltrated fault. J Geophys Res 100:22155–22171

Stauffer D, Aharony A (1994) Introduction to percolation theory, revised 2nd edition. Taylor and Francis Inc., Philadelphia, 181p

Walder J, Nur A (1984) Porosity reduction and pore pressure development. J Geophys Res 89:11539–11548

Wang C-Y, Manga M (2010) Hydrologic responses to earthquakes and a general metric. Geofluids 10:206–216

Zhang H (1999) On the ergodicity hypothesis in heterogeneous formations. Math Geol 31(1): 113–134

Zoback MD, Harjes HP (1997) Injection-induced earthquakes and crustal stress at 9 km depth at the KTB deep drilling site, Germany. J Geophys Res Solid Earth 102:18,477–18,491